Iranian Journal of Materials Science and Engineering, Vol. 23, Number 2, June 2026

RESEARCH PAPER

The Synergistic Effect of Molybdenum Dopant Content and Pressure on the Optoelectronic and Mechanical Performance of CeO_2: DFT+U Study

Karrar Hadi Mousa, Hussein Ali Jan Miran*

* *Hussein.a.j@ihcoedu.uobaghdad.edu.iq*

Department of Physics, College of Education for Pure Science-Ibn Al-Haitham, University of Baghdad, Baghdad, Iraq

Received: November 2025 **Revised: January 2026** **Accepted: May 2026**
DOI: 10.22068/ijmse.4449

Abstract: *This contribution investigates the structural, opto-electronic, and mechanical properties of cerium oxide (CeO_2) and molybdenum-included cerium oxide ($Ce_{0.75}Mo_{0.25}O_2$) under applied hydrostatic pressures of 0, 25, 50, 75, and 100 GPa. The calculations were performed using the state-of-the-art density functional theory (DFT+U). The generalized gradient approximation (GGA) supported by the PBE functional has been utilized. Initially, the lattice dimensions of the cubic CeO_2 phase account for 5.438 Å. The electronic characteristics have been inspected by assessing the band gap of the pure CeO_2 unit cell, which amounts to 3.134 eV. The computed results of lattice dimensions and band gap energy are in line with the previous experimental work. Incorporating the Mo element into the host CeO_2 lattice decreases the band gap to 2.045 eV in $Ce_{0.75}Mo_{0.25}O_2$. This value is higher when applying hydrostatic pressure till reaching 1.808 eV at 100 GPa. The projected and total density of states (PDOS) findings reveal hybridization between CeO_2 and Mo with key contributions of Ce-4f, O-2p, and Mo-3d states. Furthermore, the assessed negative formation energy magnitudes of $Ce_{0.75}Mo_{0.25}O_2$ under zero and applied hydrostatic stress evidence the thermodynamic stability, proposing the possible experimental fabrication of such a system. Under applied pressures, absorption curve examinations reveal blue shift for the inspected structures. In addition, an enhancement in the absorption spectra has been observed by shifting toward the ultraviolet (UV) wavelength region, indicating the potential applications in optoelectronic devices. The simulated findings of the mechanically elastic properties manifest ductile behavior, with an enhancement by the introduction. Consequently, this material would be a promising candidate in high-ductility applications, including protective coatings, solid oxide fuel cells, and microelectronic devices.*

Keywords: *Cerium dioxide (CeO_2), Charge distribution, Dielectric response, DFT+U, Anisotropy.*

1. INTRODUCTION

Globally, solid material oxides receive growing attention owing to their unique characteristics, rendering them involved in photovoltaic, opto-electronic, and biological applications [1–3]. Particularly, cerium oxide (CeO_2) has occupied a great area in literature because of its brilliant physical and chemical properties. These distinguished properties are motivated by the partially filled 4f orbital in Ce as well as swinging between two oxidation states of Ce^{3+} and Ce^{4+} [4–6]. CeO_2 is well-documented as an excellent cost-effective contributor to potentially assist in lessening environmental contaminations and pollutions [7, 8]. Experimentally, CeO_2 exhibits a semiconductor character with band gap energy spanning from 2.2-3.5 eV, good absorption trend in the ultraviolet area of the solar spectra with a very limited absorbance in the visible region [9, 10]. Transition metals' doping effect on the physico-chemical characteristics of the host CeO_2 crystal has been reported extensively. Particularly, Molybdenum (Mo) inclusion can optimize the catalytic activities in various reactions [11–13]. An experimental study has carried out to synthesize cerium telluride (CeTe) and Mo-CeTe films at doping levels ranging between 0.1−0.3 mol%. The results proposed that the insertion of Mo dopant into CeTe motivates band gap stretching from 1.20–1.60 eV [14]. Transition elements, including Fe, Co, Ni, and Cu, have been inserted into CeO_2 at various doping levels for reverse water gas shift (RWGS) reaction, showing promising results in CO_2 reduction [15].

The combined effect of oxygen vacancies and band gap contraction boosts the performance of the dual-ion co-doped $Ce_{0.8}Sm_{2-x}Ca_xO_{2-\delta}$ where x= 0.04, 0.08, 0.12, 0.16 [16]. The integration of Mo into the host CeO_2-supported Ni catalyst (Ni/MoCe) lattice would play a vital role in improving the surface oxygen vacancies, decreasing the particle size of Ni species, and developing the metal-support interaction [17].

L. Li et al. [18] have developed Mo-doped CeO_2 catalysts via the wet impregnation route. The catalyst demonstrated superior NO_x removal efficiency at low temperatures, exhibited strong resistance to SO_2 poisoning, and suppressed the formation of strongly adsorbed NO_x. These findings highlight Mo surface modification as a promising route to enhance both the activity and durability of CeO_2-based catalysts in environmental applications. C. Nan et al. [19] manufactured Mo-doped CeO_2 nanorods by means of a hydrothermal route under calcination. The catalyst with 5% Mo doping revealed high efficiency for the electrocatalytic nitrogen reduction reaction (NRR). This represents a fourfold improvement over pristine CeO_2 nanorods. Li Wang et al. [20] facilitated the direct reduction of CO_2 to CO using Mo-modified CeO_2. The catalyst's high efficiency was driven by the strong Mo–CeO_2 interfacial interactions. I. Díaz-Aburto et al. [21] synthesized Mo-doped CeO_2 via the combustion process at different Mo contents of 5 wt.%, 7 wt.%, and 10 wt.%. The reported Young's modulus upsurge with the Mo compositions, suggesting the highest value of 289.4 GPa at 10 wt.% Mo. In addition, Vickers microhardness displays that Mo incorporation yields a decrease in the microhardness. H. Zhang et al. [22] employed flame spray pyrolysis to examine the CH_4 non-oxidative coupling reaction over Mo-doped CeO_2, inferring high catalytic activities in this reaction [23]. A recently published research has reported that the green synthesis of CeO_2 nanoparticles coated with silver (Ag) and doped with cadmium (Cd) exhibits improved photocatalytic and antibacterial activities [24]. On the other hand, density functional theory (DFT) based studies revealed that Mo incorporation would induce modulation of the electronic properties of CeO_2. A. Bouhlala et al. [25] investigated the fundamental properties of mono and co-dopant with tungsten (W) and (Mo-W) co-doped cubic CeO_2 by means of the WIEN2k code. The band structure calculations indicated that the pure and co-doped CeO_2 exhibit semiconductor characteristics. Ultimately, the lack of pressure-dependent studies that focus on Mo-doped CeO_2 motivates us to examine the synergistic effect of 25% Mo dopant under applied hydrostatic pressures (0, 25, 50, 75, 100 GPa) on the physical properties of CeO_2.

2. COMPUTAIONAL METHODS

In the current investigation, Cambridge Serial Total Energy Package (CASTEP) based on density functional theory (DFT) was used to perform the calculations [26] in order to investigate the structural, electronic, optical, and mechanical properties of $Ce_{0.75}Mo_{0.25}O_2$ at varying hydrostatic pressures of 0, 25, 50, 75, and 100 GPa. Generalized gradient approximation (GGA) with the Perdew-Burke-Ernzerhof (PBE) functional has been utilized [27]. DFT+U is adopted to improve the accuracy of the band gap calculations, as pure DFT tends to underestimate the band gap of the studied compounds [9, 28]. Herein, U represents the Hubbard parameter, which describes the Coulomb interaction of the outer electrons of the highly correlated system [29]. Within the CASTEP program, Hubbard parameter values of U= 4.0 eV for Ce (*f*-orbital), U= 4.0 eV for Mo (*d*-orbital), and U= 4.3 eV for O (*p*-orbital) were applied. Furthermore, the calculations were performed on a conventional unit cell consisting of 4 Ce atoms and 8 O atoms. Therefore, the least concentration of Mo doping is achieved by replacing one atom of Ce, which corresponds to 25 at%. It is worth mentioning that literature has not yet reported any result on the solubility limit of Mo in CeO_2 crystal. For the strongly correlated systems, pure DFT undervalues the electronic properties (i.e. the experimental band gap energy cannot be reproduced). Literature has indicated that the hole states located at the O 2*p* state in CeO_2 is unstable [30]. As a result, U value of 4.3 eV was employed for the O *2p* state [31]. The Brillouin zone was sampled using a 4×4×4 Monkhorst-Pack k-point mesh [32] with a cut-off energy set at 600 eV. Moreover, for precise calculations, a norm-conserving pseudo potential has been implemented in the current investigation. Finally, using the "stress-strain method" within the CASTEP package, the elastic constants were calculated. The self–consistent field (SCF) tolerance is set to 10^{-6} eV/atom, and the smearing value corresponds to 0.1 eV.

3. RESULTS AND DISCUSSION

3.1. Structural Characteristics and Stability

Figure 1 presents the optimized unit cells of both pure and Mo-doped CeO_2 structures, displaying a fluorite crystal structure within the Fm-3m (#225) space group [33]. The unit cell contains four formula units, comprising four Ce and eight O atoms. In the current investigation, 25% of cerium (Ce) atoms in the unit cell are replaced with molybdenum (Mo), and the novel $Ce_{0.75}Mo_{0.25}O_2$ model adopts a primitive cubic symmetry, belonging to the Pm-3m (No. 221) space group. The optimized

[DOI: 10.22068/ijmse.4449]

pristine unit cell exhibits a lattice constant of 5.438 Å, as reported in Table 1. Previous studies have reported the lattice parameters of the optimized bulk CeO_2 as 5.44 Å [16] and 5.423 Å [35]. The integration of Mo content induces a reduction in the lattice constant of the $Ce_{0.75}Mo_{0.25}O_2$ system and attains a value of 4.894 Å under 100 GPa. This contraction arises from the substitution of a larger Ce^{4+} ion (ionic radius: 0.97 Å) with a smaller Mo^{4+} ion (0.71 Å), which shortens the interatomic distances within the crystal lattice. The reported lattice compression of the investigated structures reveals that the incorporation of dopant would lessen the unit cell volume and band gap, which would affect the material's functioning. Table 1 summarizes the charge transfer values, signifying that Ce atoms undergo charge depletion from +1.53 to +1.60 electrons, while the inclusion of Mo shows a lower charge loss of +1.27 to +1.34 electrons. Oxygen atoms gain a substantial negative charge, ranging from -0.73 to -0.78 electrons. These charge distribution patterns reveal distinct bonding characteristics. The Ce-O bonds exhibit strongly ionic behavior due to pronounced charge transfer from Ce to O, whereas the Mo-O bonds display a mixed covalent-ionic nature with predominant covalent character, evidenced by the relatively smaller charge transfer from Mo. The negative formation energy values presented in Table 1 further confirm the thermodynamic stability of the doped material under both doping and high-pressure conditions, validating its potential for practical synthesis. The formation energies of the investigated systems were computed using the following relations [36];

$$E_{f(CeO_2)} = \frac{1}{k+m}\left(E_{CeO_2}^{total} - \left(kE_{Ce}^{Bulk} + mE_{O}^{Bulk}\right)\right) \quad (1)$$

$$E_{f(Ce_{0.75}Mo_{0.25}O_2)} = \frac{1}{k+l+m}\left(E_{Ce_{0.75}Mo_{0.25}O_2}^{total} - \left(kE_{Ce}^{Bulk} + lE_{Mo}^{Bulk} + mE_{O}^{Bulk}\right)\right) \quad (2)$$

Here $E_{f(CeO_2)}$ and $E_{f(Ce_{0.75}Mo_{0.25}O_2)}$ correspond to the formation energy of the intrinsic and doped systems, while $E_{CeO_2}^{total}$ and $E_{Ce_{0.75}Mo_{0.25}O_2}^{total}$ represent the total energies of the intrinsic and Mo-doped structures. E_{Ce}^{Bulk}, E_{Mo}^{Bulk}, E_{O}^{Bulk} refer to the total energies of the most stable solid phases Ce, Mo, and O_2 bulks, respectively. These values were considered to be the chemical potentials Ce, Mo, and O_2 atoms. It is worth mentioning that to accomplish the calculations, the most stable phases of Ce and O_2 are considered as body-centered cubic (bcc) structure with space groups corresponding to Im-3m-229 and Fd-3m-227, in that order. While for the Mo phase, a hexagonal structure of P63/mmc-194 was adopted. The full counts of Ce, Mo, and O atoms in the modeled unit cell is represented by k= 3, l= 1, and m= 8, correspondingly. It follows that the evaluated formation energy of CeO_2 is -5.209 eV, indicating the thermodynamic stability of the modeled configurations as reported in Table 1. Interestingly, the computed formation energies of the simulated compounds suggest exothermic reactions reflecting their feasibility to be fabricated experimentally. While incorporating Mo dopant resulted in lessening the exothermicity. Applying hydrostatic pressures has affected the exothermicity occurring process positively as reported in Table 1.

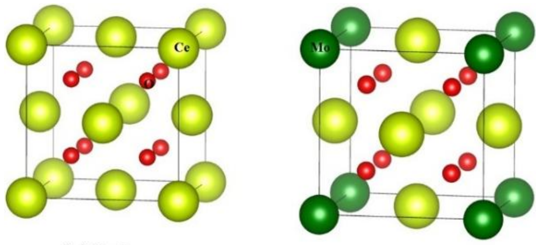

(a) CeO_2 (b) $Ce_{0.75}Mo_{0.25}O_2$

Fig. 1. The relaxed unit cells of CeO_2 and $Ce_{0.75}Mo_{0.25}O_2$ configurations. Neon yellow, dark green and red spheres signify Ce, Mo, and O atoms, respectively

Table 1. The evaluated lattice constants (Å), formation energies (eV), electronic band gaps (eV), and charge transfer (*e*) analysis of the pristine and Mo-doped CeO_2

Configurations	**lattice constants (Å) a=b=c**	**Formation energy (eV)**	**Band gap (eV)**	**Charge Transfer (e)**		
				Ce	**Mo**	**O**
CeO_2 (0 GPa)	5.438 5.481 [37] 5.39 [38]	-5.209 -8.83 [37]	3.134 3.23 [38] 3.15 [39]	1.56	–	-0.78
$Ce_{0.75}Mo_{0.25}O_2$ (0 GPa)	5.353	-4.831	2.045	1.6	1.33	-0.77
$Ce_{0.75}Mo_{0.25}O_2$ (25 GPa)	5.188	-5.168	2.058	1.58	1.34	-0.76
$Ce_{0.75}Mo_{0.25}O_2$ (50 GPa)	5.067	-5.304	1.985	1.56	1.33	-0.75
$Ce_{0.75}Mo_{0.25}O_2$ (75 GPa)	4.972	-5.415	1.910	1.54	1.3	-0.74
$Ce_{0.75}Mo_{0.25}O_2$ (100 GPa)	4.894	-5.575	1.808	1.53	1.27	-0.73

3.2. Electronic Properties Analysis

Figure 2 presents the projected and total density of states and band structure for the CeO_2 system covering an energy range from -20 eV–10 eV. Within the 0 eV–3.13 eV range, the conduction band (CB) is primarily formed by Ce-4*f* states, along with minor contributions of s and p orbitals. In contrast, the valence band (VB) expanded from -4 eV–0 eV displays dominant p-orbital character, accompanied by small contributions of d and f orbitals. Even under increasing hydrostatic pressure, $Ce_{0.75}Mo_{0.25}O_2$ continues to behave like a semiconductor, exhibiting an energy gap between 3.134 eV and 1.808 eV, as illustrated in Figure 3. At 0 GPa, the introduction of dopant would lower the energy gap from 3.134 eV (pristine CeO_2) to 2.045 eV **(**$Ce_{0.75}Mo_{0.25}O_2$). The projected and total density of states and band structure along the high symmetry points X-R in the Brillouin zone are presented in Figures 3 and 4 confirming the material's semiconductor characteristics across varying pressures.

3.3. Optical Characteristics Analysis

This investigation confirms fundamental optical performance parameters, such as light absorption, surface reflectance, optical conductivity, refractive index, dielectric performance, and energy loss are demonstrated according to these findings.

3.3.1. *Absorption coefficient and reflectance*

As shown in Figure 5, pure CeO_2 displays high UV absorption with negligible absorption in the visible light region, implying high transmittance in the visible region that motivates its use in various optical applications. Moreover, applying pressures to the $Ce_{0.75}Mo_{0.25}O_2$ configuration would induce a blue shift (moving toward shorter wavelengths) in the absorption edge as displayed in Figure 5.

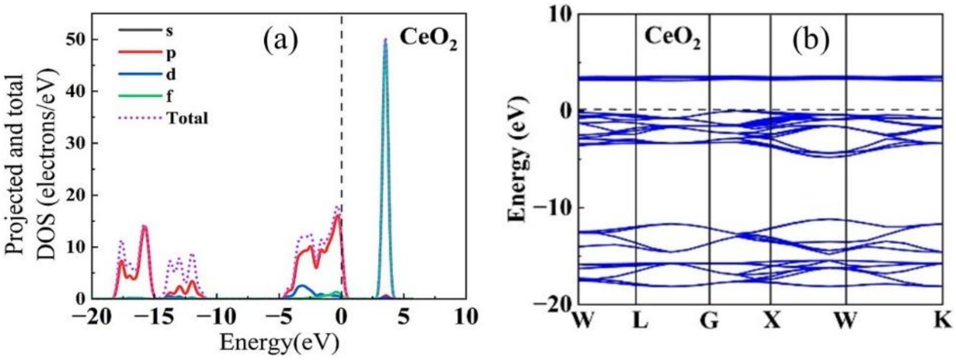

Fig. 2. a): The projected and total density of states (DOSs). b): The band structure of the pristine CeO_2 at 0 GPa.

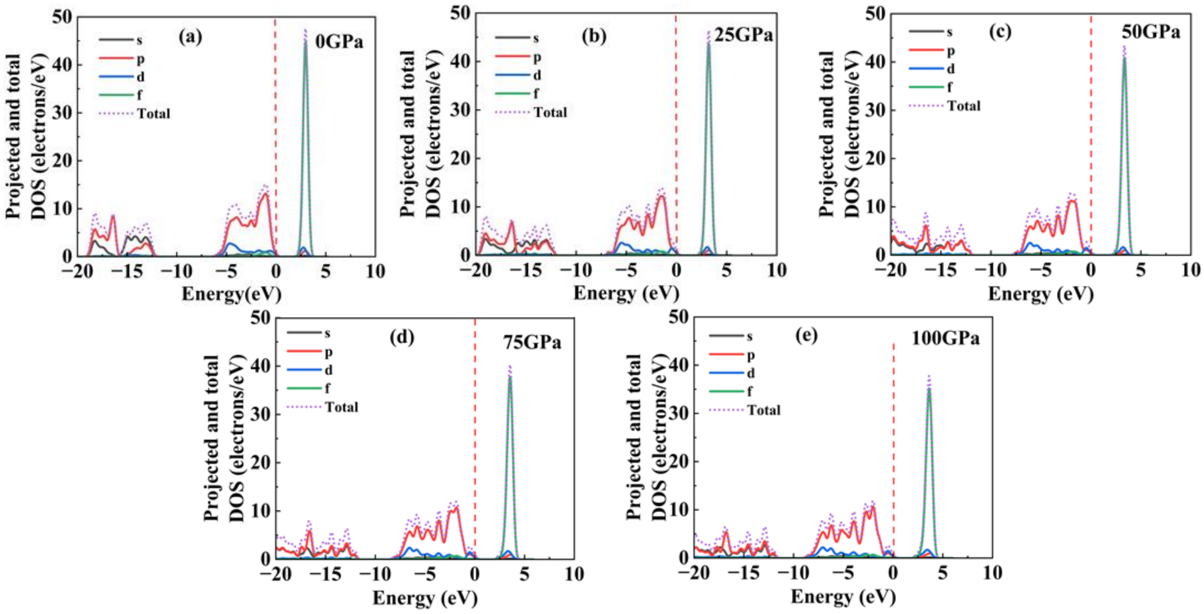

Fig. 3. The projected and total density of states (DOSs) of $Ce_{0.75}Mo_{0.25}O_2$ under the selected pressures

[DOI: 10.22068/ijmse.4449]

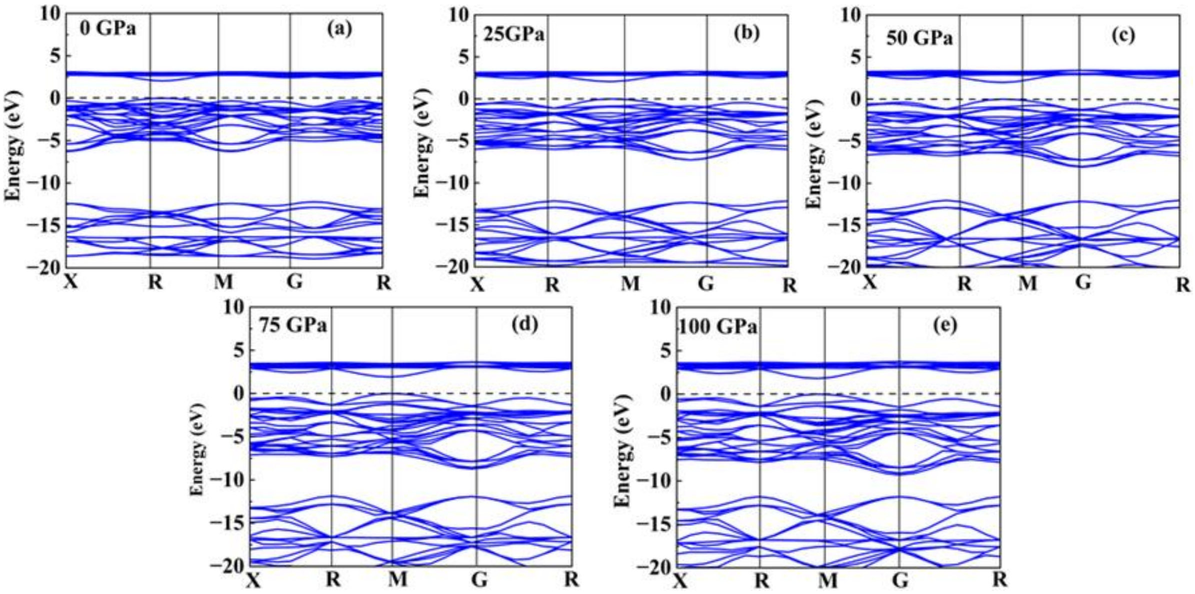

Fig. 4. The band structure of $Ce_{0.75}Mo_{0.25}O_2$ under the applied pressures

It has been demonstrated that the insertion of Mo dopant into the CeO_2 host lattice tends to reduce the band gap energy owing to the contribution of new localized electronic states (d-orbitals) in the forbidden band and thereafter absorbing photons in the visible region of the electromagnetic spectrum. It can be evidently seen that the simulated electronic and optical results are confidently correlated by initiating the absorption coefficient values from the non-zero values, which confirms the semiconducting character for the entire inspected systems [40]. All the plotted absorption coefficients proceed from non-zero values, emphasizing the semiconducting tendency of the chosen materials as depicted in Figure 5.

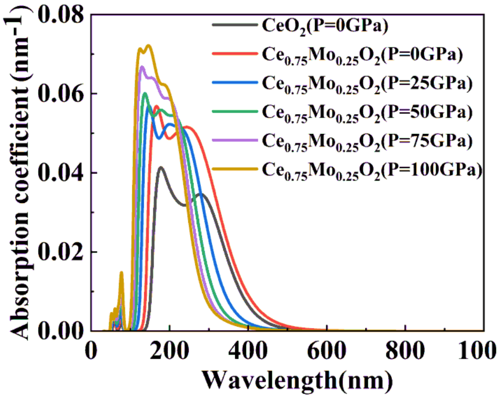

Fig. 5. Pressure-dependent absorption coefficient spectra

Figure 6 shows the reflectance spectra of the studied systems. The results indicate prominent peaks for the pure and Mo-included CeO_2 are positioned in the UV region, reflecting the higher reflectance magnitudes than those of other studied wavelength regions (i.e., visible and near IR). Among the samples, pure cerium oxide (CeO_2) exhibits the lowest reflectance, while the doped samples show slightly higher reflectance, particularly in the visible and near IR ranges. This can be attributed to the tightening of the electronic band gap energy as Mo is introduced, and hence making the material act as a metal [41]. Obviously, Mo dopant results in raising the free carriers (i.e., electrons and holes) that vibrate when absorbing visible and near-IR incident photons, and as a consequence, the emitting process increases. Furthermore, the reflectance decreases with increasing pressure, with the highest reflectance observed at 0 GPa. Lastly, it can be concluded that all the spectra of the studies have trivial reflectance values in the visible and near IR.

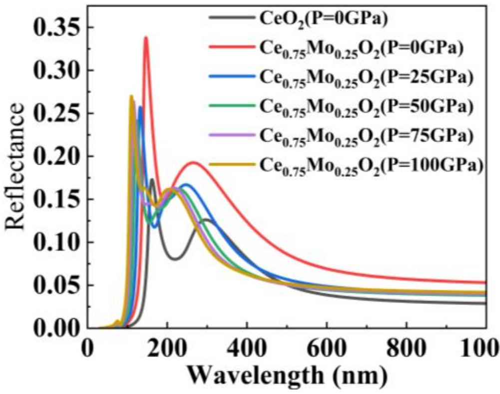

Fig. 6. Pressure-dependent reflectance spectra

[DOI: 10.22068/ijmse.4449]

[DOI: 10.22068/ijmse.4449]

3.3.2. Conductivity and insulating activities

The absorption of photons by a material leads to the emission of photoelectrons, a phenomenon known as the photoelectric effect. This phenomenon produces detectable optical conductivity, which can be theoretically modeled. Optical conductivity represents a key indicator for analyzing charge transfer mechanisms in photoactive materials. It provides a quantitative measure of electron transport dynamics in materials under optical stimulation [42]. The optical conductivity, which depends on frequency, can be represented as a complex function [43];

$$\delta(\omega) = \delta'(\omega) + i\delta''(\omega) = -i\frac{\omega}{4\pi}[\varepsilon'(\omega) + i\varepsilon''(\omega) - 1] \quad (3)$$

The real and imaginary components of conductivity are given by $\delta'(\omega)$ and and $i\delta''(\omega)$, whereas the dielectric function is expressed in terms of its real part $\varepsilon'(\omega)$ and imaginary part $\varepsilon''(\omega)$. As demonstrated in Figure 7, the optical conductivity of pure CeO_2 exhibits measurable values in the visible light spectrum, with the imaginary component reflecting transparency behavior that aligns with the observed absorption characteristics. Figure 8 illustrates that doping and applying pressure (0-100 GPa) can induce transparency in pure CeO_2 within the visible light spectrum. This effect occurs when molybdenum (Mo) atoms replace cerium (Ce) atoms at a doping ratio of 25% in the system.

As revealed in Figure 9, the energy loss spectra of the pristine CeO_2 at zero pressure show a predominant peak at about 175 nm before sharply declining to zero at higher wavelengths. For $Ce_{0.75}Mo_{0.25}O_2$, applying pressure shifts the loss energy spectra toward shorter wavelengths. Concisely, these remarkable findings propose negligible energy loss in the visible region of electromagnetic radiation.

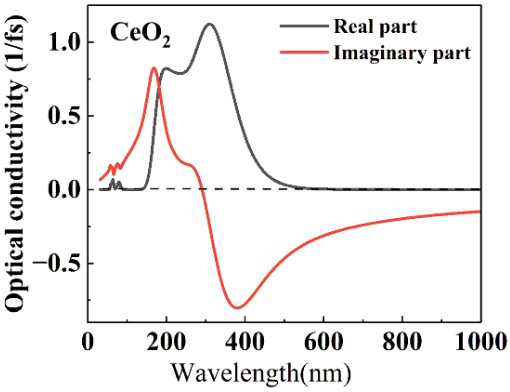

Fig. 7. The optical conductivity of CeO_2 at 0 GPa

3.3.3. Dielectric function

In materials science, the dielectric response of a substance plays a considerable role in predicting its capability to store electrical energy, which is crucial for applications such as capacitors. Consisting of real $\varepsilon_1(\omega)$ and imaginary $\varepsilon_2(\omega)$ components, the dielectric function $\varepsilon(\omega)$ captures electronic polarization and photon absorption coefficient, respectively, according to the expression below [37];

$$\varepsilon(\omega) = \varepsilon_1 + i\varepsilon_2(\omega) \quad (4)$$

Figure 10 depicts the dielectric responses of CeO_2. The real and imaginary dielectric components spectra suggest sharp peaks at around 425 nm and 325 nm, respectively.

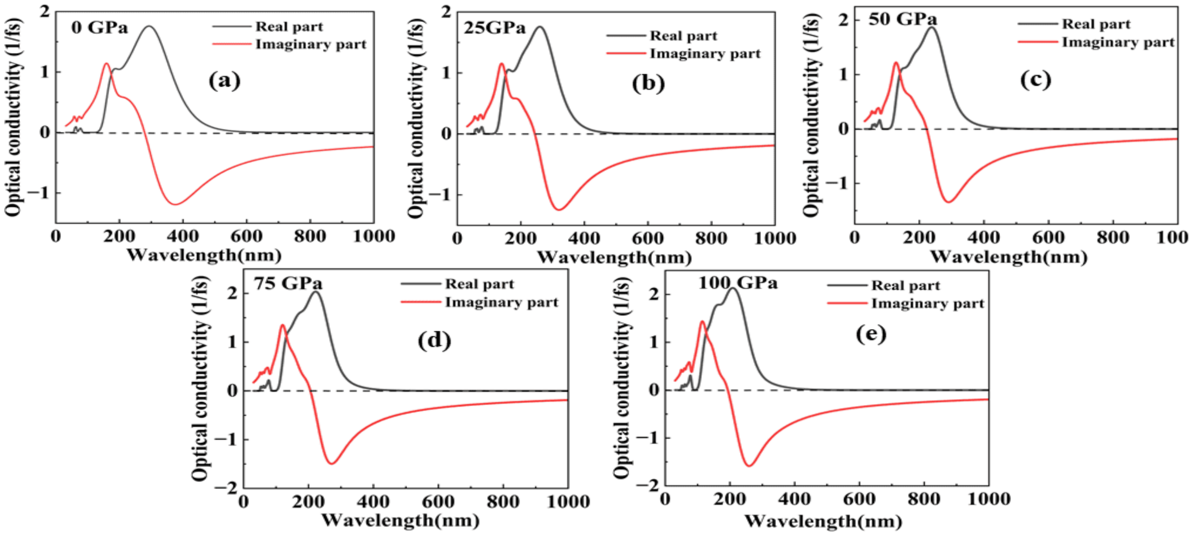

Fig. 8. The pressure-dependent optical conductivity of $Ce_{0.75}Mo_{0.25}O_2$

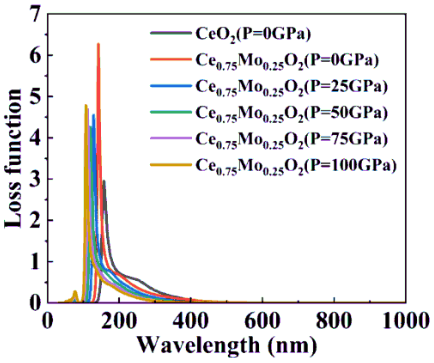

Fig. 9. Pressure-dependent energy loss function of CeO_2 and $Ce_{0.75}Mo_{0.25}O_2$

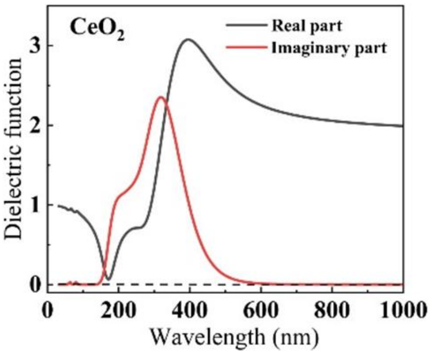

Fig. 10. The calculated dielectric function of CeO_2 at 0 GPa

However, these peaks are shifted toward shorter wavelengths of $Ce_{0.75}Mo_{0.25}O_2$ under the selected pressures, as illustrated in Figure 11 [44].

3.3.4. Complex refractive Index

It has been reported that CeO_2 thin films display a high refractive index (*n*) of 2.33 at 632.8 nm [45]. Nonetheless, the simulated refractive index value at the ground state energy level corresponds to approximately 1.5 at the same wavelength. In view of that, the imaginary component of refractive index is typically represented by extinction coefficients (*k*), which is given by the relation;

$$k = \frac{\varepsilon_2}{2n} \quad (5)$$

Figure 12 displays the evaluated refractive index (*n*) and imaginary part (*k*) of the CeO_2 crystal at 0 GPa. It is obviously identified from the figure that the maximum *k* value discloses 0.73 at 325 nm; this value drops at higher wavelengths. Figure 13 displays the combined effect of Mo insertion and applied pressures on the host CeO_2 crystal lattice. The *n* and *k* spectra of $Ce_{0.75}Mo_{0.25}O_2$ configurations demonstrate a gradual shift toward shorter wavelengths under applied pressures, suggesting reduced transparency. This finding strongly indicates its potential utilization in optoelectronic applications.

3.4. Mechanical Properties Analysis

Each crystal system is characterized by a specific number of elastic constants (C_{ij}). For instance, the cubic crystal system has only three independent elastic constants, which are C_{11}, C_{12}, and C_{44}. This reduction in the number of constants arises from the high degree of symmetry in cubic crystals; the more symmetric the structure, the fewer independent elastic constants are needed to describe its mechanical behavior.

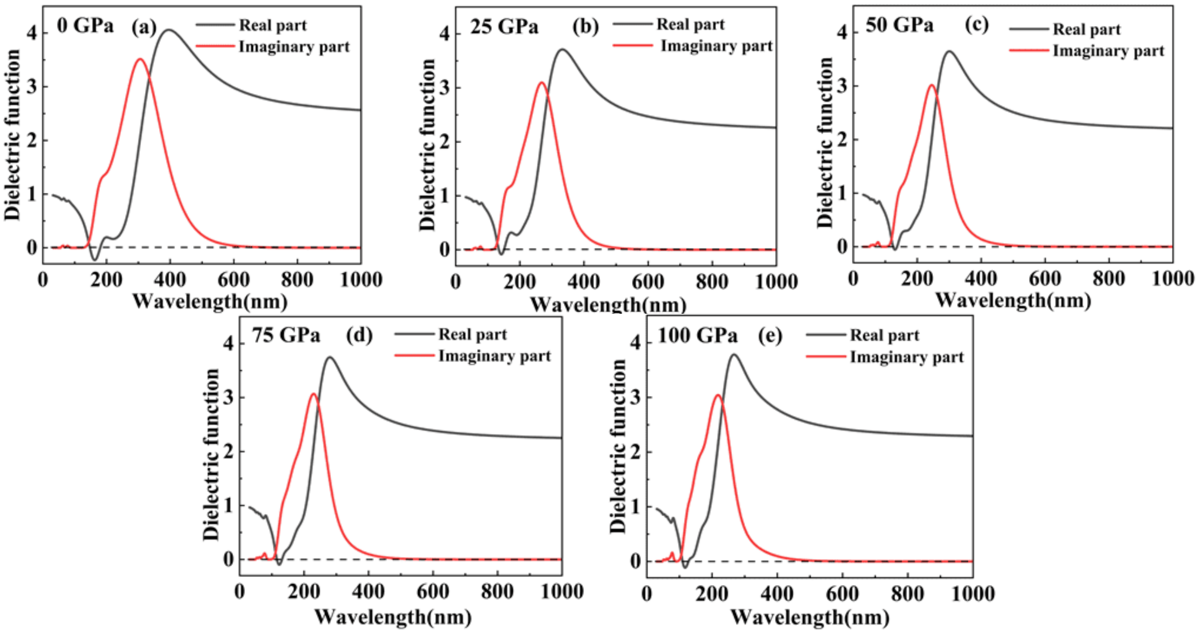

Fig. 11. The calculated dielectric function of $Ce_{0.75}Mo_{0.25}O_2$ at varying pressures

[DOI: 10.22068/ijmse.4449]

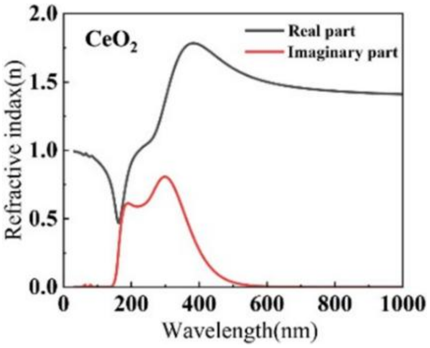

Fig. 12. Complex refractive index of CeO_2 at 0 GPa

These constants are vital for analyzing the mechanical properties of materials, which is crucial to evaluating their suitability for industrial applications, especially under extreme environmental conditions. By calculating these constants in CASTEP of CeO_2 and $Ce_{0.75}Mo_{0.25}O_2$ under applied pressures, key parameters can be determined. These parameters offer valuable insights for predicting material properties such as hardness, deformation resistance, and brittleness versus ductility. For the cubic system, to ensure mechanical stability, the following standard criteria must be accomplished [46];

$(C_{11} + 2C_{12}) > 0; C_{44} > 0; (C_{11} - C_{12}) > 0; C_{11} > 0$

As evidenced by the data in Table 2, the results meet the necessary conditions for mechanical stability. This is reinforced by the behavior of C11, which quantifies the material's resistance to compressive or tensile stresses along the principal crystallographic directions. The value of C_{11} serves as a measure of the material's stiffness. We observed a systematic rise in C_{11} with both doping concentration and applied pressure, demonstrating improved resistance to deformation. This enhancement stems from the replacement of relatively weaker Ce–O bonds with more robust Ce–Mo bonds. The increase in C_{44} indicates stronger shear deformation resistance. This trend parallels the enhancement in bulk modulus (B), which quantifies the material's resistance to volume change under pressure, as detailed in a previous study [47];

$$B = \frac{C_{11}+2C_{12}}{3} \qquad (6)$$

Doping and hydrostatic pressure both lead to elevated bulk modulus values, confirming improved bulk stiffness in the modified materials. The observed behavior indicates strong interatomic bonding. Shear modulus (G) can be calculated using the following equation [46];

$$G_V = \frac{1}{5}(C_{11} - C_{12} + (3C_{44})) \qquad (7)$$

$$G_R = \frac{5C_{44}(C_{11}-C_{12})}{4C_{44}+3(C_{11}-C_{12})} \qquad (8)$$

$$G = \frac{G_V + G_R}{2} \qquad (9)$$

For pure CeO_2 at 0 GPa, the measured shear modulus reached 75.024 GPa, demonstrating significant inherent hardness. However, introducing 0.25 content of Mo enhances this value to 85.905 GPa under identical conditions. Interestingly, when pressure is elevated while maintaining a fixed doping concentration, the material's hardness shows a substantial improvement, reaching 143.215 GPa at 100 GPa.

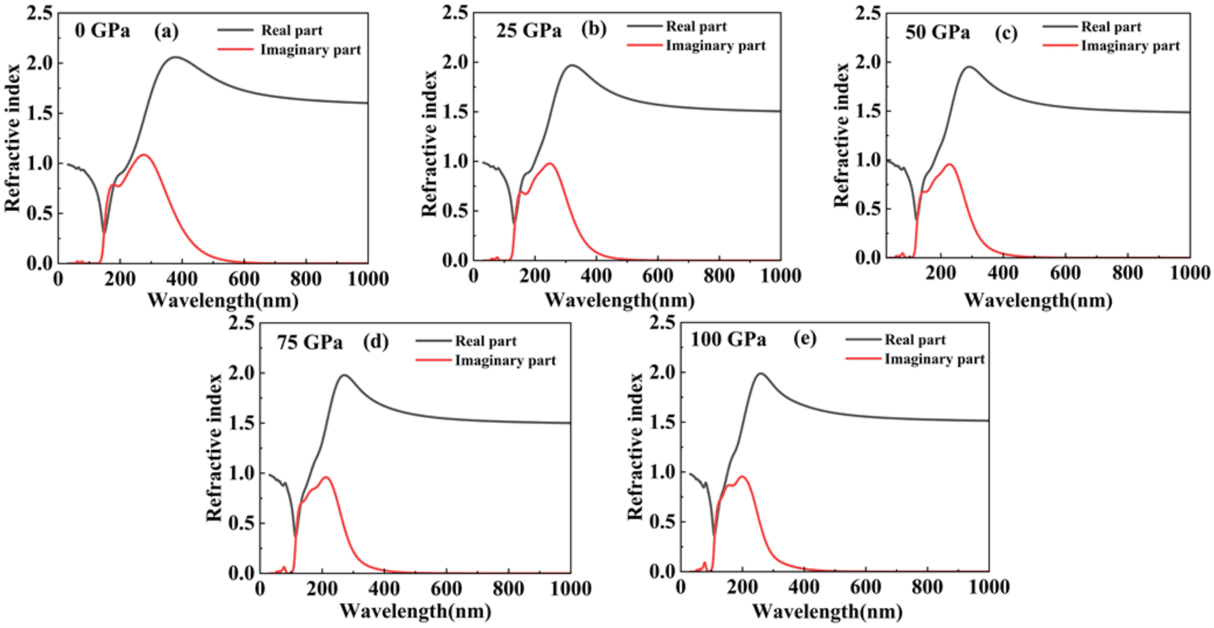

Fig. 13. Complex refractive index of $Ce_{0.75}Mo_{0.25}O_2$ at different pressures

[DOI: 10.22068/ijmse.4449]

[DOI: 10.22068/ijmse.4449]

These results highlight the synergistic effects of doping and pressure on mechanical properties. To assess a material's ductile versus brittle behavior, the Pugh ratio (B/G) must be evaluated. The Pugh ratio (B/G) serves as a key indicator of a material's ductile or brittle nature. A ratio exceeding 1.75 signifies ductile behavior, while values below this threshold indicate brittleness [48]. The findings indicate that the material exhibits ductile behavior, with its ductility further enhanced by doping. As a result, this material holds potential for use in high-ductility applications, including protective coatings, solid oxide fuel cells, nuclear industries, and microelectronic devices [29]. Another key parameter that differentiates ductile from brittle materials is Poisson's ratio (ν). Typically, a value greater than 0.3 confirms ductile behavior, suggesting the material's ductility. This ratio can be calculated using the following expression [46];

$$\nu = \frac{3B-2G}{6B+2G} \qquad (10)$$

The Cauchy pressure (C_{12}–C_{44}) was calculated for all samples. The positive values listed in Table 3 confirm the material's ductile behavior and metallic bonding nature. The drastic increments in elastic stiffness coefficient values (C_{12}) with increasing pressure validate the significant increase in Cauchy pressure of the $Ce_{0.75}Mo_{0.25}O_2$ structure. Furthermore, the reduction in lattice parameters when applying pressures, as shown in Table 1, leads to lessening the interatomic distances and, thereafter, enhancing the ductility trend of the material being strongly correlated with enhancing the Cauchy pressure. Additionally, the low compressibility values (1/B), where B is the bulk modulus, further indicate the material's hardness and ductility. Similarly, Zener's anisotropy ratio (A) reflects mechanical anisotropy when its value is less than one. These values provide insight into the material's stiffness characteristics, with the results presented in Table 3 based on the following relation [37];

$$A = \frac{2C_{44}}{C_{11}-C_{12}} \qquad (11)$$

The high Young's modulus (E) values presented in Table 2 serve as key indicators of the material's enhanced hardness. These results clearly demonstrate how doping contributes to improved hardness under increasing pressure. Young's modulus was determined using the following equation [46];

$$E = \frac{9BG}{3B+G} \qquad (12)$$

Before applying pressures, the bulk modulus B increased with introducing 25% Mo content, signifying that Mo dopants result in a strong resistance to volume change for CeO_2. Moreover, shear modulus G and Young's modulus E are augmented, inferring that Mo dopants motivate the resistance against elastic and shear deformations of the CeO_2 host lattice. Table 2 indicates that Young's modulus is increased by introducing 10 wt.% Mo content and its experimentally measured value by Díaz-Aburto et al. [21] was 289.4 GPa.

The formability ratio (μ_m), with values exceeding 1.75 (Table 2), confirms the material's excellent workability and shaping potential.

Table 2. The predicted elastic properties of CeO_2 and $Ce_{0.75}Mo_{0.25}O_2$. Elastic stiffness constants Cij (GPa), Bulk modulus B (GPa), Shear modulus G (GPa), Young's modulus E (GPa), Poisson's ratio v, and machinability index μ_m, and Vickers' hardness H_V

Crystal structures	C_{11}	C_{12}	C_{44}	B	G	E	v	μ_m	H_V
CeO_2 (0GPa)	347.378	96.73	52.513	180.279	75.024	197.675	0.317	3.433	8.919
	341 [37]	102 [37]	56 [37]	181 [37]	77 [37]	202 [37]	0.314 [37]	3.23 [37]	6.15 [37]
	353.6 [49]	101.4 [49]	52.9 [49]	185.5 [49]	75.6 [49]	199 [49]	0.321 [49]	3.51 [49]	5.75 [49]
$Ce_{0.75}Mo_{0.25}O_2$ (0GPa)	363.233	106.972	65.394	192.392	85.905	224.327	0.305	3.433	9.378
$Ce_{0.75}Mo_{0.25}O_2$ (25GPa)	472.759	186.429	92.552	281.872	110.296	292.711	0.326	2.942	9.256
$Ce_{0.75}Mo_{0.25}O_2$ (50GPa)	595.386	268.671	93.660	377.576	117.236	318.722	0.359	3.045	8.711
$Ce_{0.75}Mo_{0.25}O_2$ (75GPa)	642.058	352.159	113.108	448.792	124.924	342.952	0.372	4.031	8.295
$Ce_{0.75}Mo_{0.25}O_2$ (100GPa)	742.341	437.137	137.279	538.872	143.215	394.683	0.377	3.967	7.597

Table 3. The estimated mechanical properties of the systems under consideration

Crystal structures	Zener's anisotropy (A)	Compressibility (1/B)	Pugh ratio (B/G)	Cauchy pressure (C_{12}-C_{44})
CeO_2 (0GPa)	0.419 0.467 [37]	0.005	2.402	44.217 46 [37]
$Ce_{0.75}Mo_{0.25}O_2$ (0GPa)	0.510	0.0051	2.239	41.577
$Ce_{0.75}Mo_{0.25}O_2$ (25GPa)	0.646	0.003	2.555	93.876
$Ce_{0.75}Mo_{0.25}O_2$ (50GPa)	0.573	0.002	3.220	175.010
$Ce_{0.75}Mo_{0.25}O_2$ (75GPa)	0.780	0.0022	3.592	239.051
$Ce_{0.75}Mo_{0.25}O_2$ (100GPa)	0.899	0.001	3.762	299.858

This property exhibits a positive correlation with applied pressure, making the material particularly suitable for industrial applications demanding high formability, such as solar cell manufacturing. The formability ratio was determined via the following equation;

$$\mu_m = \frac{B}{C_{44}} \qquad (13)$$

The calculated Vickers hardness (H_V) values demonstrate the material's significant hardness, indicating strong resistance to penetration. This property makes it particularly valuable for applications requiring durable surfaces. The hardness values were derived theoretically using the following relation [46];

$$H_V = 2\left(\frac{G^3}{B^2}\right)^{0.583} \qquad (14)$$

4. CONCLUSIONS

This study aims at systematically investigating the electronic, structural stability, optical, and mechanical properties of CeO_2 and $Ce_{0.75}Mo_{0.25}O_2$ under pressures by means of Density Functional Theory (DFT). At 0 GPa, the band gap energy decreased from 3.134 eV of the pristine CeO_2 to 2.045 eV of $Ce_{0.75}Mo_{0.25}O_2$. With increasing hydrostatic pressures, the band gap of $Ce_{0.75}Mo_{0.25}O_2$ exhibited a gradual shrinkage until reaching 1.808 eV at 100 GPa. Overall, the synergistic effect of 25% Mo doping and applied pressure reduces the band gap by over 1.3 eV, enhances UV absorption, and motivates optoelectronic industries. Moreover, the analysis of the mechanical characteristics results improves the ductility while increasing the stiffness of CeO_2, with an enhancement at Mo content insertion and hence nominating this material to be involved in high-ductility applications, such as protective coatings, solid oxide fuel cells, and microelectronic devices. Finally, for materials engineering, more systematic studies are promising toward investigating the effect of co-doping with multiple transition metals on the CeO_2 crystal.

REFERENCES

[1] G. Kumaravel, S. Kirthiga, M. M. H. Al Shekaili, and Q. H. S. A. AL Othmani, A Solar Photovoltaic Performance Monitoring and Statistical Forecasting Model Using a Multi-Layer Feed-Forward Neural Network and Artificial Intelligence, Baghdad Sci. J. 21, 1868 (2024).

[2] S. S. Al-Awadi, A. A. Ramadhan, F. T. Ibrahim, and A. K. Abbood, Optical and structural properties of titanium dioxide papered by dc magneto-sputtering as a NO_2 gas sensor, Iraqi J. Sci. 61, 2562 (2020).

[3] D. S. Shaker, N. K. Abass, and R. A. U. Ulwali, Preparation and study of the Structural, Morphological and Optical properties of pure Tin Oxide Nanoparticle doped with Cu, Baghdad Sci. J. 19, 24 (2022).

[4] R. Kumar, V. K. Gupta, M. Khosya, S. Singh, and U. Kumar, Comparative computational and experimental insights into the structural, electrical, and biological properties of CeO_2 fluorite ceramics, Sci. Rep. 15, 1 (2025).

[5] J. Graciani, A. M. Marquez, J. J. Plata, Y. Ortega, N. C. Hernandez, A. Meyer, C. M. Zicovich-Wilson, and J. F. Sanz, Comparative study on the performance of hybrid DFT functionals in highly correlated oxides: The case of CeO_2 and Ce_2O_3, J. Chem. Theory Comput. 7, 56 (2011).

[6] H. A. Miran, Z. N. Jaf, I. H. Khaleel, and A. A. Alkhafaji, Photocatalytic and optical performances of CeO_2 by substitution of titanium, Phys. Chem. Res. 9, 553 (2021).

[7] S. S. Mahmood, B. A. Hasan, and A. F. Rauuf, Effect of Manganese Oxide Doping of Tin Oxide Thin Films on the Optical and Structural Properties, Iraqi J. Sci. 65, 3754 (2024).

[DOI: 10.22068/ijmse.4449]

[8] B. M. Reddy and A. Khan, Nanosized CeO_2–SiO_2, CeO_2–TiO_2, and CeO_2–ZrO_2 mixed oxides: influence of supporting oxide on thermal stability and oxygen storage properties of ceria, Catal. Surv. from Asia 9, 155 (2005).

[9] H. A. Miran, M. Altarawneh, Z. N. Jaf, M. M. Rahman, M. H. Almatarneh, and Z.-T. Jiang, Influence of the variation in the Hubbard parameter (U) on activation energies of CeO_2-catalysed reactions, Can. J. Phys. 98, 385 (2020).

[10] S. A. Ansari, M. M. Khan, M. O. Ansari, S. Kalathil, J. Lee, and M. H. Cho, Band gap engineering of CeO_2 nanostructure using an electrochemically active biofilm for visible light applications, RSC Adv. 4, 16782 (2014).

[11] Z. N. Jaf, M. Altarawneh, H. A. Miran, and Z. T. Jiang, Geometries, electronic properties and stability of molybdenum and tungsten nitrides low-index surfaces, Mater. Res. Express 5, 126402 (2018).

[12] Z. N. Jaf, H. A. Miran, I. H. Khaleel, and K. A. Jasim, Assessing the optoelectronic performance of d-orbital doped cubic HfO_2: The case of W, Nb, and Mo, Optik (Stuttg). 264, (2022).

[13] Z. N. Jaf, M. Altarawneh, H. A. Miran, M. H. Almatarneh, Z. T. Jiang, and B. Z. Dlugogorski, Catalytic Hydrogenation of p-Chloronitrobenzene to p-Chloroaniline Mediated by γ-Mo_2N, ACS Omega 3, 14380 (2018).

[14] I. L. Ikhioya, S. O. Aisida, I. Ahmad, and F. I. Ezema, The effect of molybdenum dopant on rare earth metal chalcogenide material, Chem. Phys. Impact 7, 100269 (2023).

[15] Y. Yu, W. Xia, A. Yu, D. S. A. Simakov, and L. Ricardez-Sandoval, Transition-Metal-Doped CeO_2 for the Reverse Water-Gas Shift Reaction: An Experimental and Theoretical Study on CO_2 Adsorption and Surface Vacancy Effects, ChemSusChem. 18, e202400681 (2025).

[16] X. Hao, G. Wei, H. Zhang, S. Tan, and G. Ji, Defect chemistry-regulated design of doping CeO_2 with the enhanced high-temperature low infrared emissivity property, Mater. Today Nano 30, 100614 (2025).

[17] X. Zou et al., Molybdenum-doping promoted surface oxygen vacancy of CeO_2 for enhanced low-temperature CO_2 methanation over Ni-CeO_2 catalysts, Appl. Surf. Sci. 661, 160087 (2024).

[18] L. Li, C. Ge, J. Ji, W. Tan, X. Wang, X. Wei, K. Guo, C. Tang, and L. Dong, Effects of different methods of introducing Mo on denitration performance and anti-SO_2 poisoning performance of CeO2, Chinese J. Catal. 42, 1488 (2021).

[19] C. Nan, H. Yang, F. Gao, N. Gao, W. Zhou, H. Du, and Z. Liang, Effects of Molybdenum Doping on the Enhanced Electrocatalytic Nitrogen Reduction Reaction Performance of CeO_2 Nanorods: Theoretical and Experimental Investigations, ChemPlusChem. 88, e202300023 (2023).

[20] L. Wang, X. Du, Y. Yi, H. Wang, M. Gul, Y. Zhu, and X. Tu, Plasma-enhanced direct conversion of CO_2 to CO over oxygen-deficient Mo-doped CeO_2, Chem. Commun. 56, 14801 (2020).

[21] I. Díaz-Aburto, F. Gracia, and M. Colet-Lagrille, Mo-doped CeO_2 Synthesized by the Combustion Method for Carbon-Air Solid Oxide Fuel Cell (CA-SOFC) Applications, Fuel Cells 19, 147 (2019).

[22] H. Zhang, Y. Su, N. Kosinov, and E. J. M. Hensen, Non-oxidative coupling of methane over Mo-doped CeO_2 catalysts: Understanding surface and gas-phase processes, Chinese J. Catal. 49, 68 (2023).

[23] Y. Yu, T. Wang, X. Jiang, K. Chen, Q. Wu, Y. Zhang, D. Shi, and H. Li, Advances in the Preparation Strategies and Structural Regulation for CeO_2-Containing Electrocatalysts Applied to the Anodes of Direct Alcohol Fuel Cells: A Comprehensive Review, J. Mater. Chem. A. 13, 20143-20175 (2025).

[24] P. S. Parab, A. A. Pawanoji, K. R. Jarhad, and A. S. Pawar, Harnessing the Effects of Cd-Doped and Ag-Coated CeO_2 (IV) Nanoparticles for Enhanced Nitrophenol Reduction, Photocatalytic Degradation, and Other Potential Biological Applications, BioNanoSci. 15, 1 (2025).

[25] A. Bouhlala, M. Doghmane, W. T. Halais, and S. Chettibi, The impact of molybdenum and tungsten co-doping on the physical properties of CeO_2: First-principles calculations, Mod. Phys. Lett. B 38, (2024).

[26] R. Munirathnam, H. C. Manjunatha, Y. S. Vidya, L. Seenappa, K. N. Sridhar, T. C. S.

[DOI: 10.22068/ijmse.4449]

Girisun, T. Sharmila, and S. V. R. Murugan, Optical limiting and two-photon absorption in transition metal and rare earth-doped CeO_2 nanoparticles, Phys. B Condens. Matter 711, 417226 (2025).

[27] J. P. Perdew, K. Burke, and M. Ernzerhof, Generalized Gradient Approximation Made Simple, 1996.

[28] Z. N. Jaf, H. A. Miran, M. M. Rahman, A. Amri, and Z.-T. Jiang, DFT+U investigation on high pressure properties of monoclinic CuO, Can. J. Phys. 102, 316 (2024).

[29] S. Lutfalla, V. Shapovalov, and A. T. Bell, Calibration of the DFT/GGA+U method for determination of reduction energies for transition and rare earth metal oxides of Ti, V, Mo, and Ce, J. Chem. Theory Comput. 7, 2218 (2011).

[30] T. El-Achari, F. Goumrhar, L. B. Drissi, and R. A. Laamara, Structural, electronic and magnetic properties of Mn doped CeO_2: An ab-initio study, Phys. B Condens. Matter 601, 412443 (2021).

[31] B. Huang, R. Gillen, and J. Robertson, Study of CeO_2 and its native defects by density functional theory with repulsive potential, J. Phys. Chem. C 118, 24248 (2014).

[32] H. J. Monkhorst and J. D. Pack, Special points for Brillouin-zone integrations, Phys. Rev. B 13, 5188 (1976).

[33] J. L. Lu, H. J. Gao, S. Shaikhutdinov, and H. J. Freund, Morphology and defect structure of the CeO_2(1 1 1) films grown on Ru(0 0 0 1) as studied by scanning tunneling microscopy, Surf. Sci. 600, 5004 (2006).

[34] H. S. Batool, M. J. I. Khan, I. Taj, J. Ahmad, M. Yousaf, and M. Yousaf, DFT investigations of structural, electronic, magnetic, and optical properties of CeO_2-X (X= Mo/Cr) and Mo-Cr co-doped CeO_2 for optoelectronic applications, Solid State Commun. 385, 115499 (2024).

[35] Y. Xue, D. Tian, D. Zhang, C. Zeng, Y. Fu, K. Li, H. Wang, and Y. Tian, The mechanism of photocatalyst and the effects of co-doping CeO_2 on refractive index and reflectivity from DFT calculation, Comput. Mater. Sci. 158, 197 (2019).

[36] J. L. F. Da Silva, M. V. Ganduglia-Pirovano, J. Sauer, V. Bayer, and G. Kresse, Hybrid functionals applied to rare-earth oxides: The example of ceria, Phys. Rev. B- Condens. Matter Mater. Phys. 75, 045121 (2007).

[37] K. M. Hossain, S. Kumar Mitro, S. A. Moon, M. Mozahar Ali, S. Chandra, and M. A. Hossain, Influence of heavy Hf doping in CeO_2: Prediction on various physical properties, Results Phys. 37, 105569 (2022).

[38] Z. Liu, B. Wang, and C. Cazorla, Mechanical and electronic properties of CeO_2 under uniaxial tensile loading: A DFT study, Materialia 15, 101050 (2021).

[39] O. S. Polezhaeva, N. V. Yaroshinskaya, and V. K. Ivanov, Synthesis of nanosized ceria with controlled particle sizes and bandgap widths, Russ. J. Inorg. Chem. 52, 1184 (2007).

[40] M. Q. Saadon and H. A. Miran, Computational modeling study on the physical properties of Pd doped $BaTiO_3$ perovskite, Comput. Condens. Matter 39, e00906 (2024).

[41] F. T. Geldasa and F. B. Dejene, Effects of S Doping and Oxygen Vacancy on the Physical Properties of Rutile TiO_2 for Photocatalysis Applications Based on Density Functional Theory Study, Materials (Basel). 18, 1688 (2025).

[42] H. A. Miran, Z. N. Jaf, M. Al Tarawneh, M. M. Rahman, A. T. Al-Bayati, and E. M-T. Salman, First-Principles Analysis of Cr-Doped $SrTiO_3$ Perovskite as Optoelectronic Materials, Iran. J. Mater. Sci. Eng. 20, 1 (2023).

[43] B. Peng, H. Zhang, H. Shao, Y. Xu, R. Zhang, and H. Zhu, The electronic, optical, and thermodynamic properties of borophene from first-principles calculations, J. Mater. Chem. C 4, 3592 (2016).

[44] Z. N. Jaf, Z.-T. Jiang, H. A. Miran, and M. Altarawneh, Thermo-elastic and optical properties of molybdenum nitride, Can. J. Phys. 94, 902 (2016).

[45] F.-C. Chiu and C.-M. Lai, Optical and electrical characterizations of cerium oxide thin films, J. Phys. D. Appl. Phys. 43, 075104 (2010).

[46] H. A. Miran and Z. N. Jaf, A Systematic DFT Study on the Optoelectronic and Elastic Characteristics of H-Induced $KMnF_3$ Perovskite, Brazilian J. Phys. 55, (2025).

[47] H. A. Miran, M. Altarawneh, H. Widjaja, Z. N. Jaf, M. Mahbubur Rahman, J. P. Veder, B. Z. Dlugogorski, and Z. T. Jiang,

[DOI: 10.22068/ijmse.4449]

Thermo-mechanical properties of cubic lanthanide oxides, Thin Solid Films 653, 37 (2018).

[48] R. J. Sabri and Z. N. Jaf, Optoelectronic characteristics of sulfur-doped LaAlO3 at hydrostatic pressures: A computational study, Comput. Condens. Matter 44, e01054 (2025).

[49] H. Jia, M. Li, X. Li, B. Ren, X. Liu, and J. Zhao, Effects of nonmetal (F, Si, B, and P) doping on the electronic structure and elastic properties of CeO_2: A first-principles study, J. Alloys Compd. 666, 419 (2016).

[DOI: 10.22068/ijmse.4449]